

# Highly-sensitive superconducting quantum interference proximity transistor

Alberto Ronzani, Carles Altimiras,<sup>\*</sup> and Francesco Giazotto  
*NEST, Istituto Nanoscienze-CNR and Scuola Normale Superiore, I-56127 Pisa, Italy*

We report the design and implementation of a high-performance superconducting quantum interference proximity transistor (SQUIPT) based on aluminum-copper (Al-Cu) technology. With the adoption of a thin and short copper nanowire we demonstrate full phase-driven modulation of the proximity-induced minigap in the normal metal density of states. Under optimal bias we record unprecedentedly high flux-to-voltage (up to  $3\text{ mV}/\Phi_0$ ) and flux-to-current (exceeding  $100\text{ nA}/\Phi_0$ ) transfer function values at sub-Kelvin temperatures, where  $\Phi_0$  is the flux quantum. The best magnetic flux resolution (as low as  $500\text{ n}\Phi_0/\sqrt{\text{Hz}}$  at 240 mK, being limited by the room temperature pre-amplification stage) is reached under fixed current bias. These figures of merit combined with ultra-low power dissipation and micrometer-size dimensions make this mesoscopic interferometer attractive for low-temperature applications such as the investigation of the magnetization of small spin populations.

PACS numbers: 85.35.-p, 85.25.Am, 85.25.Cp, 85.25.Dq, 74.45.+c, 74.50.+r, 74.78.Na

The superconducting quantum interference proximity transistor [1] (SQUIPT) is a two terminal device based on a tunnel junction between a superconducting “probe” electrode and a normal metal wire inserted in a superconducting loop, see Fig. 1(a). Owing to *proximity effect* [2] the clean electric contact between the normal and the superconducting metal leads to the appearance of a phase-dependent minigap in the electronic density of states (DOS) of the normal metal [3]. Yet, once proximized, the latter establishes a weak coupling [4] between the superconducting electrodes in contact with it, so that the whole superconductor-normal metal-superconductor (SNS) complex operates as a Josephson junction [5]. An external magnetic field threading the loop therefore modulates the amplitude of the minigap by establishing a definite phase difference across the Josephson junction as a consequence of flux quantization in the closed superconducting ring [6, 7].

SNS weak-links offer the possibility to realize superconducting couplings unachievable by Josephson tunnel junctions, for instance, providing non sinusoidal current-phase relation in the short junction length limit [5], or achieving a  $\pi$ -state by driving the weak-link into non-equilibrium conditions [8]. In SQUIPTs, the SNS weak-link is exploited so that the electronic DOS of the metallic wire is modulated [3, 9, 10] by externally driving the magnetic flux. Therefore SQUIPTs can be considered as a magnetic analog of semiconductor field effect transistors, and can be exploited as sensitive magnetic flux sensors. Being based on mesoscopic quantum effects, they bear technological similarities with Single Electron Transistors (SETs) used as charge sensors [11]: they require being operated at sub-Kelvin temperatures and are characterized by moderately high output impedances limiting their bandwidth unless radiofrequency matching techniques are used [12]. Despite these limitations, they are well worth the effort since their performance in terms of flux sensitivity and power dissipation has no technolog-

ical counterpart. For instance, ultimate magnetic flux resolution values as low as  $1\text{ n}\Phi_0/\sqrt{\text{Hz}}$  below 1K (where  $\Phi_0 = h/2e \simeq 2.067 \times 10^{-15}\text{ Wb}$  is the flux quantum) have been predicted for SQUIPTs based on large energy-gap superconducting materials such as vanadium [13]. This makes them attractive for low-temperature applications such as the investigation of the magnetization of small spin populations.

Here we report the realization and characterization of a SQUIPT based on the Al-Cu technology which shows record flux-to-voltage transfer function values (up to  $\simeq 3\text{ mV}/\Phi_0$ ), leading to a magnetic flux resolution  $\Phi_N \simeq 500\text{ n}\Phi_0/\sqrt{\text{Hz}}$  at 240 mK in the near DC frequency range and being limited by the voltage noise of the room temperature preamplification stage.

The earliest proof-of-concept realization [1] of a SQUIPT described a device based on a copper wire of length  $L = 1.5\text{ }\mu\text{m}$  proximized by a thin aluminum loop spanning a surface of  $\approx 120\text{ }\mu\text{m}^2$ . These figures resulted in the SNS junction being in the *long* diffusive limit (*i.e.*,  $L \gg \xi_0$ , where  $\xi_0$  is the coherence length), entailing modest minigap modulation amplitudes ( $\approx 10\text{ }\mu\text{eV}$ ) under optimal current bias. In subsequent attempts aiming at increasing the response of the device up to its predicted intrinsic limits [13], the length of the N wire has been reduced to bring the SNS junction in the *short* regime, where the amplitude of the proximized minigap can approach that of the “parent” superconductor. These devices [14] succeeded in achieving wider induced minigap values ( $\approx 130\text{ }\mu\text{eV}$ ), but suffered from hysteresis stemming from self-induced magnetic screening caused by the high critical current magnitude typical of short metallic weak-links. This shortcoming has recently been lifted by reducing the cross-section of the copper wire while keeping it in the short-junction limit ( $L \approx 250\text{ nm}$ ) therefore allowing to reach a sizeable magnetic flux responsivity, with an estimated  $\approx 50\text{ }\mu\text{eV}$  minigap modulation amplitude, *i.e.*,  $\approx 36\%$  of the full induced minigap width

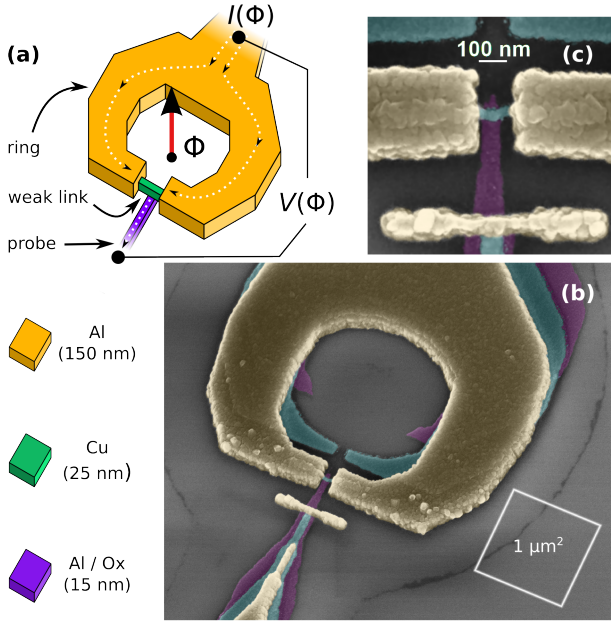


FIG. 1. (a) Functional schematic of a SQUIPT device, realized by tilted evaporation of metallic thin films through a suspended resist mask defined by electron-beam lithography. The first evaporation (purple layer) consists in 15 nm of aluminum (Al), subsequently oxidized to form an AlOx tunnel barrier. The second evaporation (green layer) consists in 25 nm of copper (Cu) realizing the normal metal nanowire. Finally, 150 nm of Al (dark yellow) are evaporated to form the superconducting loop (having inner diameter  $\simeq 1.7 \mu\text{m}$ ) as well as the electrodes in clean electric contact with the Cu film. In the schematic  $\Phi$  is the magnetic flux linked to the superconducting loop,  $I(\Phi)$  and  $V(\Phi)$  are respectively the current flowing through and the voltage difference across the device. (b) Tilted scanning electron micrograph showing the complete SQUIPT loop. (c) Scanning electron micrograph centered on the Cu nanowire region. The interelectrode spacing is  $\simeq 140 \text{ nm}$ ; the width of the nanowire is  $\simeq 30 \text{ nm}$ . The tunnel probe is  $\simeq 60 \text{ nm}$ -wide at the interface with the Cu weak-link.

deduced from the differential conductance measurements [15].

The cause for incomplete minigap modulation lies in non-ideal phase bias of the weak-link. In the limit of negligible magnetic screening originating from the geometric self-inductance of the loop, the effective phase difference imposed to the weak-link by flux quantization is affected by the competition between the kinetic inductance of the superconducting loop and that of the weak-link (respectively  $\mathcal{L}^S$  and  $\mathcal{L}^{WL}$ ). Complete phase-bias, corresponding to high phase gradient developed across the Cu nanowire, is only possible in the limit  $\mathcal{L}^S/\mathcal{L}^{WL} \ll 1$  [3]. The difficulty in achieving this regime originates from the short-junction nature of the weak-links which, apart from the aforementioned high critical current values, also show at low temperature a non-sinusoidal current-phase rela-

tionship  $I^{WL}(\phi)$ . Both effects [5, 16] suppress the magnitude of  $\mathcal{L}^{WL} = (\Phi_0/2\pi)(\partial I^{WL}/\partial \phi)^{-1}$  as the value of the phase difference  $\phi$  approaches  $\pi$ , where the sharpest response is expected [13]. In the present SQUIPT we show that a complete phase bias can be achieved in a junction approaching the short limit by realizing a copper wire having a nanoscale cross-section (thus maximizing  $\mathcal{L}^{WL}$ ) while at the same time having a compact superconducting aluminum loop characterized by low normal-state resistance (therefore minimizing both the kinetic and geometric components of  $\mathcal{L}^S$ ). As a consequence of the full minigap modulation in the proximized weak-link, we obtain record magnetic flux responsivity figures, both in current and voltage biased setups.

Figure 1(b) shows the scanning electron micrograph of a typical SQUIPT device, fabricated by standard electron-beam lithography on a suspended bilayer resist mask [17] (1000 nm copolymer / 100 nm polymethylmethacrylate) on top of an oxidized silicon substrate. An initial 15-nm-thick Al layer is deposited at  $40^\circ$  via electron-beam evaporation in ultra-high vacuum conditions ( $\simeq 10^{-9}$  Torr), and subsequently exposed to a pure  $\text{O}_2$  atmosphere (37 mTorr for 300 s) to obtain the tunnel probe electrode. The normal metal nanowire is realized by evaporating a 25-nm-thick Cu layer at  $20^\circ$ . Finally, a 150-nm-thick Al film in clean contact with the latter layer is deposited at zero angle to implement the superconducting loop, designed to have an internal diameter  $\simeq 1.7 \mu\text{m}$ . The device core [see Fig. 1(c)] shows an interelectrode spacing  $L \simeq 140 \text{ nm}$ , while the copper nanowire is 30 nm-wide and overlaps the lateral superconducting electrodes for  $\simeq 400 \text{ nm}$  per side. The width of the tunnel probe electrode is  $\simeq 60 \text{ nm}$ . Based on previous measurement on Cu nanowires of similar cross-section [18], we estimate the ratio  $L/\xi_0 = L\sqrt{\Delta_r/\hbar D_{Cu}} \approx 1.1$  which confirms the frame of the intermediate-short junction regime. Above,  $\Delta_r \simeq 185 \mu\text{eV}$  is the energy gap in the superconducting ring and  $D_{Cu} \simeq 55 \text{ cm}^2/\text{s}$  is the diffusion coefficient for our Cu nanowire. The yield of such simple fabrication scheme is about 20%, being mostly limited by the mechanical stability of the suspended polymethylmethacrylate mask defining the loop.

The SQUIPT magneto-electric characterization was performed in a filtered  $^3\text{He}$  cryostat for several temperatures in the range  $0.24 - 0.85 \text{ K}$ . Current response under voltage bias was measured in a two-wire configuration with a commercial current preamplifier (DL Instruments model 1211) as a function of the magnetic flux generated by a magnetic field applied orthogonally to the plane of the substrate. The current response shows periodicity with respect to the applied magnetic field density with period  $B_0 = \Phi_0/A_{eff} \approx 6.2 \text{ G}$ , where  $A_{eff} \approx 3.3 \mu\text{m}^2$  is consistent with the area enclosed by the ring of the SQUIPT.

Figure 2(a) shows the current vs voltage  $I(V_{\text{bias}})$  characteristics recorded at the base temperature ( $T =$

240 mK), for selected equally-spaced values of the applied magnetic flux ranging from  $\Phi = 0$  to  $\Phi = \Phi_0/2$ . At zero flux (fully open minigap) the characteristic shows a behaviour resembling that of a tunnel junction between superconductors with different energy gaps. By increasing the magnetic field the minigap closes, until the characteristic is similar to that of a *NIS* junction at  $\Phi = \Phi_0/2$ . From these data we estimate the 15-nm-thick aluminum probe to be characterized by a superconducting gap  $\Delta_{pr} \approx 235 \mu\text{eV}$  and a tunnel resistance  $R_T \approx 55 \text{ k}\Omega$ . The curves are consistent with a maximum minigap amplitude  $\varepsilon_g(\Phi = 0) \approx 145 \mu\text{eV}$ , a value which corresponds approximately to 78% of the energy gap in the superconducting ring. Figure 2(b) shows the theoretical Bardeen-Cooper-Schrieffer (BCS)-like profile [19] of the DOS in the probe junction  $\rho_{pr}(E) = \left| \text{Re} \left( \frac{E+i\gamma}{\sqrt{(E+i\gamma)^2 - \Delta_{pr}^2}} \right) \right|$  where  $\gamma/\Delta_{pr} = 10^{-3}$  accounts for energy smearing due to finite quasiparticle lifetime [20, 21]. Panels in figure 2(c) show the theoretical DOS in the weak link  $\bar{\rho}_{WL}(E)$ , spatially averaged over the probe width. The latter DOS has been obtained by solving numerically the 1-D Usadel equations [22, 23] with parameters  $L/\xi_0 = 1.1$ ,  $\Delta_r = 185 \mu\text{eV}$  and assuming perfect interface transmissivity between the ring and the wire, for  $\Phi = \{0, 0.25, 0.5\}\Phi_0$ .

The upper inset of Fig. 2(a) shows a magnified view of the flux dependent features appearing at low bias. The latter can be attributed to a weak Josephson coupling between the proximized nanowire and the probe electrode, and their complete suppression at  $\Phi = \Phi_0/2$  is a further indication of the full modulation of the minigap. A close inspection of the current vs voltage characteristics in Fig. 2(a) indicates that the measured current modulation is able to reach peak-to-peak amplitudes as large as 4 nA. On the other hand, when biased at fixed current, the amplitude of the corresponding voltage modulation approaches  $\varepsilon_g/e$ .

The lower inset in Fig. 2(a) shows a blow-up of the characteristics at the onset of quasiparticle conduction. Here the current is non monotonic as a consequence of the appreciable thermal population of the quasiparticle states in the proximized nanowire resulting in additional conduction when  $V_{\text{bias}} = [\Delta_{pr} - \varepsilon_g(\Phi)]/e$ . This bias configuration shifts the chemical potentials of the tunnel junction electrodes so that the singularity in the empty DOS of the probe electrode is energetically aligned to the thermally excited quasiparticles in the copper nanowire. In the following, we adopt the term “singularity-matching peak” to refer to this particular transport feature, in analogy to  $S_1IS_2$  systems [24]. The tunnel resistance value obtained in the fabrication process is compatible with the optimal input load impedance of both voltage and current preamplifiers. In the following we consider both voltage-biased and current-biased setups.

Current vs flux (*i.e.*, at fixed voltage bias) response fig-

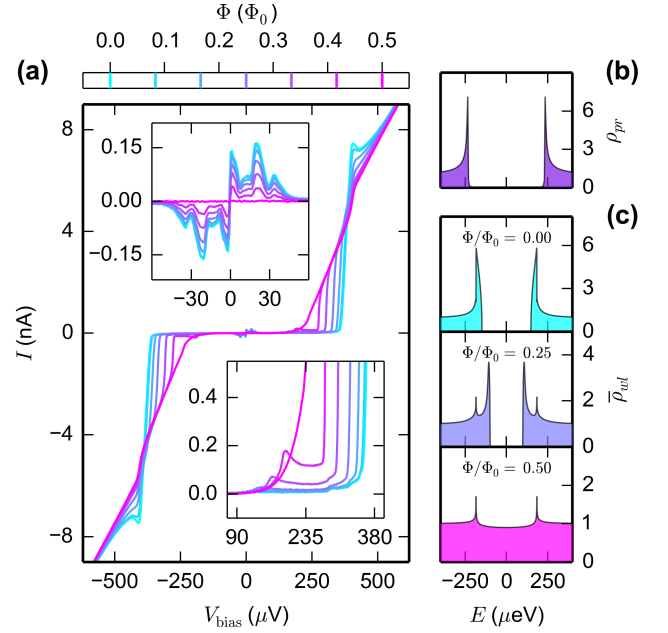


FIG. 2. (a) SQUIPT current vs voltage characteristics recorded at 240 mK for 7 equally-spaced magnetic flux values ranging from  $\Phi = 0$  to  $\Phi = \Phi_0/2$ . The upper inset shows a magnification of the low-voltage bias range, where weak phase-dependent supercurrent features appear at fixed voltage values. The lower inset shows a magnification of the onset of quasiparticle conduction, where the voltage dependence of the current can be non-monotonic as a consequence of thermally-activated transport. This is particularly evident (at finite temperature) when the minigap starts to be suppressed by the magnetic flux. (b) Theoretical BCS density of states  $\rho_{pr}(E)$  of the superconducting probe ( $\Delta_{pr} = 235 \mu\text{eV}$ ). (c) Theoretical local density of states  $\bar{\rho}_{wl}(E)$  in the proximized weak-link averaged over the probe width for three different values of the applied magnetic flux.  $\bar{\rho}_{wl}(E)$  was obtained by the numerical solution of the 1-D Usadel equations assuming  $L = 1.1 \xi_0$ , and full transparency at the interfaces.

ures have been obtained by numerical differentiation with respect to the magnetic flux of the  $I(\Phi, V_{\text{bias}})$  characteristics [Figure 3(a)] at fixed  $V_{\text{bias}}$ . Figure 3(b) shows the absolute value of the base temperature flux-to-current transfer function  $|\partial I(V_{\text{bias}}, \Phi)/\partial \Phi|$  as a colormap. In this context the transfer function map indicates sharp response (due to the abrupt onset of quasiparticle conduction) reaching values as high as  $108 \text{ nA}/\Phi_0$ , over a wide range of the bias parameters in both flux:  $\Phi \in [0.35 \div 0.45 \Phi_0]$ , and voltage bias:  $V_{\text{bias}} \in [275 \div 310 \mu\text{V}]$ . This high sensitivity (approximately four times higher than the best-performing devices so far [15]) originates from both a lower tunnel probe resistance and a full modulation of the minigap. In addition, the maximum flux-to-current responsivity level, is only moderately suppressed by increasing the temperature [see Fig. 3].

Voltage vs flux characteristics, recorded at 240 mK for a few selected values of the current bias in the vicinity

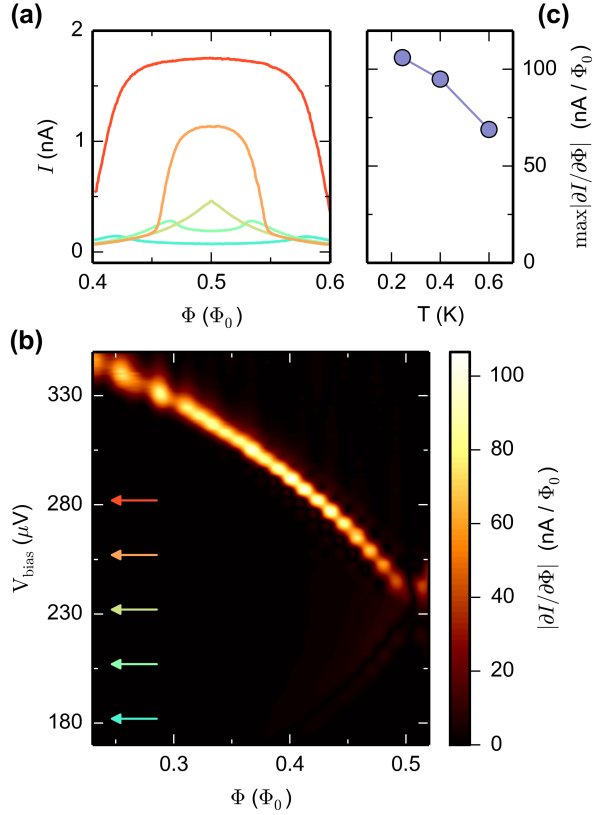


FIG. 3. (a) Current vs flux characteristics measured at 240 mK for fixed voltage bias (from bottom to top,  $V_{\text{bias}} = 182, 212, 232, 252, 282 \mu\text{V}$ ). (b) Color plot of the absolute value of the flux-to-current transfer function ( $|\partial I / \partial \Phi|$  vs  $V_{\text{bias}}$  and  $\Phi$ ) obtained by numerical differentiation of the  $I(\Phi)$  curves measured at 240 mK. Arrows indicate in corresponding colors the voltage bias values for the characteristics plotted in panel (a). (c) Temperature dependence of the maximum absolute value of the flux-to-current transfer function.

of the maximal response ( $I_{\text{bias}} = 435 \text{ pA}$ ,  $\Phi \simeq 0.5 \Phi_0$ ) are shown in Fig. 4(a). The absolute value of the relative flux-to-voltage transfer function is plotted as a colormap in Fig. 4(d). At low current bias the non-monotonicity of the current vs voltage characteristics [see the bottom inset of Fig. 2(a)] results into bistable voltage configurations, giving rise to hysteretic behaviour and limiting the useful bias range for a SQUIPT used as a linear sensor. The non-monotonicity originating from the singularity-matching peak can, in principle, be limited by lowering the electron temperature beyond the base temperature of our cryostat. This can be achieved by using dilution refrigerators but also with the adoption of integrated on-chip electronic coolers [25, 26] relying on the same fabrication technique. On the other side, the supercurrent peaks give rise to a similar electric bistability [see Fig. 2(a), top inset] and are expected to increase in magnitude at lower temperatures (when not countered

by lower transparency of the tunnel barrier) and will ultimately limit the current bias range available for linear response.

Notably, the electric bistability provided by the singularity-matching peak could instead be exploited for operating the SQUIPT as a threshold detector. In this configuration, the flux is applied in the close vicinity of a switching point [e.g.,  $I_{\text{bias}} = 335 \text{ pA}$  and  $\Phi = 0.48 \Phi_0$  in Fig. 4(d)], so that flux variations crossing the threshold given by the switching point yield a voltage step response (whose amplitude may be  $\approx 50 \mu\text{V}$ ) within a timescale corresponding to the relaxation time of the measurement setup. Such scheme can be useful for sampling the probability distribution function of a noisy magnetic flux source.

We now discuss the SQUIPT sensitivity when operated as a linear flux sensor. Inspection of the flux-to-voltage transfer function [shown as a colormap in Fig. 4(d)] reveals that the current-biased setup allows for a high responsivity ( $\approx 1 \text{ mV}/\Phi_0$ ) over a rather broad flux and current bias range, with a peak value of  $\approx 3 \text{ mV}/\Phi_0$ , located at  $\Phi = 0.495 \Phi_0$  and  $I_{\text{bias}} = 435 \text{ pA}$ . This working point lies just outside of the hysteretic region [marked with magenta lines in Fig. 4(d)] and it is thus a suitable point for linear operation of the detector.

While compatible with earlier results [15], such a high voltage transfer function may seem surprising. Indeed, the detailed theoretical investigation of the SQUIPT performance in the short junction limit (where analytic calculations can be performed) carried in [13], predicted maximal transfer functions of about  $3.1 \Delta_r / e \Phi_0$  around  $\Phi = 0.5 \Phi_0$ , which can be traced back to the flux dependence of the minigap. Extrapolating this limit to our moderately-short SNS junction, *i.e.*, assuming the same scaling but replacing  $\Delta_r$  with the measured minigap  $\varepsilon_g = 145 \mu\text{eV}$ , one would expect a response of about  $450 \mu\text{eV}/\Phi_0$ , which is 6 times smaller than the maximum value obtained in the experiment. The reason for the observed higher response stems from the contribution of the singularity-matching peak, ignored in [13], which bends the non-hysteretic  $V(\Phi, I_{\text{bias}})$  characteristics in the vicinity of  $\Phi_0/2$  and  $V = \Delta_{pr}/e$ , resulting in a sharper voltage response. This feature can be easily reproduced by using a simplified model which holds in the short-junction limit as described in [13], with the replacement  $\Delta_r \leftrightarrow \varepsilon_g$ .

Figure 4(c) presents a contour plot of the  $I(\Phi, V_{\text{bias}})$  dataset obtained with the above theoretical model in the vicinity of  $eV_{\text{bias}} = \Delta_{pr} = 235 \mu\text{eV}$  and  $\Phi/\Phi_0 = 0.5$  at  $T = 240 \text{ mK}$ . The white lines correspond to calculated current isolines, who strongly resemble those observed in the actual measured  $I(\Phi, V_{\text{bias}})$  characteristics [see Fig. 4(b)]. Although rather idealized, the model provides a satisfactory reproduction of the physical mechanism underlying the observed high responsivity. Furthermore, a close match between the measured  $V(\Phi, I_{\text{bias}})$  response curves and the current isolines can be appreciated in the



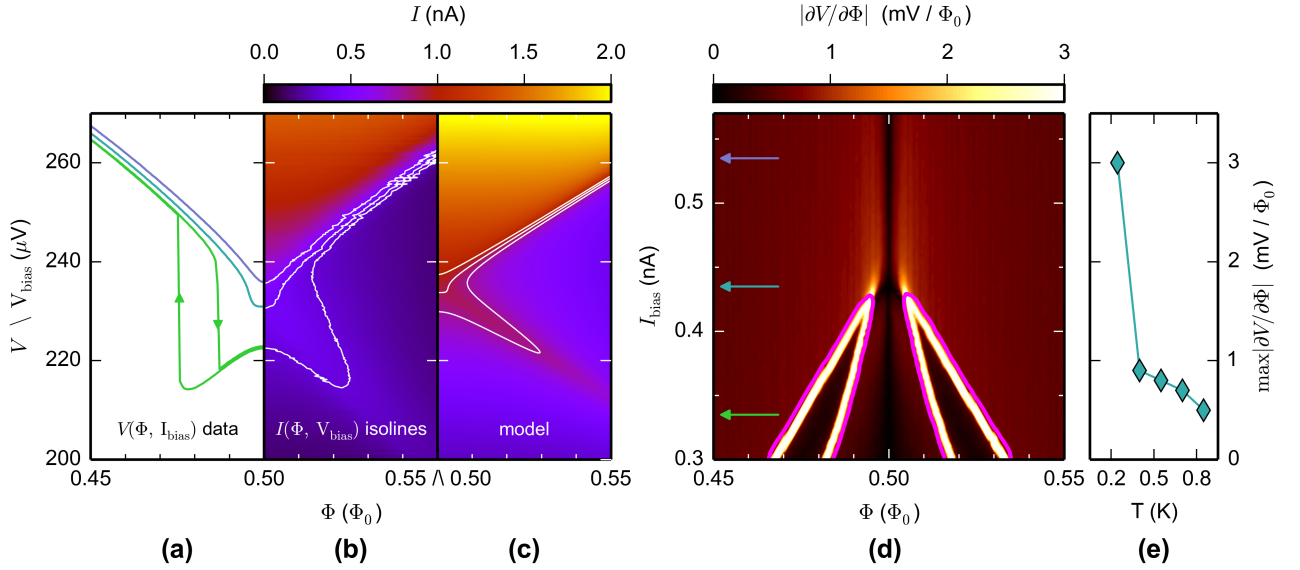


FIG. 4. **(a)** Voltage vs flux characteristics measured at 240 mK for fixed current bias (from bottom to top,  $I_{\text{bias}} = 335, 435, 535$  pA). **(b)** Color plot showing the measured  $I(V_{\text{bias}}, \Phi)$  dataset; the current isolines match the characteristics shown in panel (a). The reentrant shape of the lowest current isoline is at the origin of the hysteresis displayed in the corresponding  $V(\Phi, I_{\text{bias}})$  characteristic [green trace in panel (a)]. **(c)** Color plot of the theoretical current vs  $V_{\text{bias}}$  and  $\Phi$  calculated for a SQUIPT device based on a weak-link in the short regime. **(d)** Color plot of the absolute flux-to-voltage transfer function ( $|\partial V / \partial \Phi|$  vs  $V_{\text{bias}}$  and  $\Phi$ ) obtained by numerical differentiation of  $V(\Phi)$  curves measured at 240 mK. Hysteresis originating from the non-monotonicity of the current vs voltage characteristics [see lower inset of Fig. 2(a)] can be appreciated for  $I_{\text{bias}} < 435$  pA. The associated switching events are marked by green arrows in panel (a). Magenta lines mark the hysteretic regions in the colormap. Arrows indicate in corresponding colors the current bias values for the characteristics plotted in panel (a). **(e)** Temperature dependence of the maximum absolute value of the flux-to-voltage transfer function.

juxtaposition of panels (a,b) in Fig. 4, therefore corroborating the identification of physical origin of the high flux-to-voltage responsivity we observe.

In particular, three regimes can be recognized, depending on the magnitude of the quasiparticle current. Low-current regime [corresponding to the green trace and arrow in Fig. 4(a,d)] is characterized by hysteresis originating from the singularity-matching peak bistability, which is evident in the reentrant shape of the low-current isolines in Fig. 4(b,c). Conversely, in the high-current limit [exemplified by the blue trace and arrow in Fig. 4(a,d)] no hysteresis can be found, but the magnetic flux responsivity is only moderate. The optimal regime for sensitivity [represented by the cyan trace and arrow in Fig. 4(a,d)] emerges in the smooth transition between the two above-mentioned limits. This latter regime features the highest value of the flux-to-voltage transfer function, but no hysteresis.

The temperature dependence of the maximum value of the transfer function is displayed in Fig. 4(e). The substantial enhancement observed at lower temperature is due to the abrupt character of the thermal suppression of the singularity-matching peak appearing in the current vs voltage characteristics, which allows to access the optimal current-bias range required for the sharpest

voltage response.

Our device has been designed to show that high transfer function values can be obtained in SQUIPTs based on Al-Cu technology. The intermediate value of the impedance of the device ( $R_T = 55$  k $\Omega$ ), allows sensitive operation of the interferometer in both voltage-biased and current-biased setups. However, given the significant capacitive load present in the filtered lines of our refrigerator setup, the current-biased measurement scheme shows better performance thanks to the superior common-mode noise rejection properties of differential voltage preamplification.

Figure 5 shows an assessment of the noise performance of the SQUIPT as a magnetic flux sensor obtained at 240 mK by measuring the power spectral density (PSD) of voltage fluctuations recorded at the output of battery powered differential voltage preamplifiers (NF Corporation model LI-75A). Two identical preamplification units are connected to the two independent analog to digital converter (ADC) channels of a spectrum analyzer (HP model 89410A), which computes the PSD of each channel as well as the cross-correlated spectral density (CSD) between the two. The latter quantifies the amount of noise which shows as correlated in the two ADC channels, and sets an upper limit to the estimate of the intrinsic noise

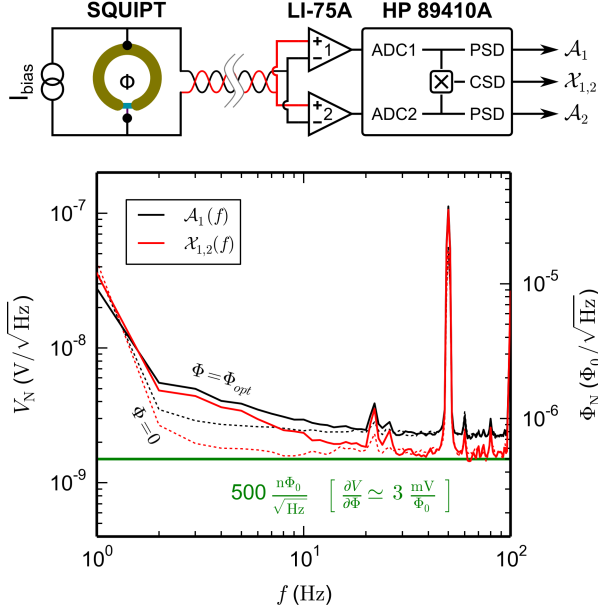


FIG. 5. Noise level measurement in a current bias mode at 240 mK. The schematic displayed on top summarizes the measurement setup, in which the signal from the SQUIPT is split and fed symmetrically into two battery-powered differential voltage preamplifiers (NF Corporation model LI-75A). The outputs from the preamplifiers are independently sampled by two analog to digital converters (ADC) in a digital spectrum analyzer (HP model 89410A), which computes the power spectral density (PSD,  $\mathcal{A}_i$ , black traces) for each ADC channel as well as the cross spectral density (CSD,  $\mathcal{X}_{1,2}$ , red traces) between the two. The resulting data is expressed in voltage noise referred to the input of the preamplifiers ( $V_N$ , in  $V/\sqrt{\text{Hz}}$  units). Continuous lines indicate traces recorded at optimal current and flux bias, where the transfer function is maximal ( $3 \text{ mV}/\Phi_0$ ). The right vertical axis shows the values for the magnetic flux resolution ( $\Phi_N$ ) under these conditions. The  $500 \text{ n}\Phi_0/\sqrt{\text{Hz}}$  white noise level is shown as a green horizontal line. Dotted lines indicate control traces recorded with optimal current bias at  $\Phi = 0$  (zero transfer function and comparable differential resistance).

figures for the measurement setup. The SQUIPT device is operated in the current-bias mode with  $I_{\text{bias}} = 435 \text{ pA}$ . The spectral densities (both PSD and CSD) are expressed in amplitude units ( $V_N$ , in  $V/\sqrt{\text{Hz}}$ ); the expected bandwidth of the measurement setup ( $\simeq 20 \text{ Hz}$  when tuned for high sensitivity) is here limited by the significant capacitance of the filtered measurement lines ( $\simeq 90 \text{ nF}$ ).

The continuous-line traces in Fig. 5 were acquired with the device tuned for maximum sensitivity ( $|\partial V/\partial \Phi|_{\text{max}} = 3 \text{ mV}/\Phi_0$  and  $\Phi_{\text{opt}} = 0.495 \Phi_0$ ). In these conditions, besides some spurious noise peaks, the input-referred white noise level for the preamplifiers (black trace) approaches the nominal limit for this model ( $2 \text{ nV}/\sqrt{\text{Hz}}$ ), while the cross-correlated white noise level

(red trace) reaches values as low as  $1.5 \text{ nV}/\sqrt{\text{Hz}}$ . Control traces, shown in Fig. 5 as dotted lines, were acquired with  $I_{\text{bias}} = 435 \text{ pA}$  but zero magnetic flux (and hence zero transfer function, yet similar output differential resistance). They differ from the maximum-sensitivity traces for the absence in the  $2 - 20 \text{ Hz}$  frequency range of a  $1/f$  slope whose level (assuming a field-to-voltage coefficient  $A_{\text{eff}}|\partial V/\partial \Phi|_{\text{max}} \simeq 4.8 \text{ V/T}$ ) is consistent with the expected magnetic low-frequency noise found in unshielded rooms in urban environment (typically in the  $0.1 - 1 \text{ nT}/\sqrt{\text{Hz}}$  range at  $10 \text{ Hz}$  [27]).

The white-noise floor displayed in the CSD traces is significantly lower than the corresponding levels from the single-channel PSD, meaning that the room-temperature preamplification stage is here limiting the noise performance of the measurement setup. The cross-correlated voltage white-noise floor sets an upper limit to the magnetic flux resolution achievable by our measurement setup,

$$\Phi_N = \frac{V_N}{|\partial V/\partial \Phi|} \simeq 500 \text{ n}\Phi_0/\sqrt{\text{Hz}}.$$

In spite of the relatively simple measurement equipment used, this noise figure is already comparable with state-of-the-art SNS SQUIDS interferometers equipped with custom cryogenic preamplification readout systems [28, 29].

Significant improvement in terms of magnetic flux resolution would be possible with the adoption of a cryogenic preamplification to reduce the measurement noise down to  $0.3 \text{ nV}/\sqrt{\text{Hz}}$  [30]: assuming noise figures still dominated by the readout [13], we can expect a 5-fold increase in flux sensitivity making the present SQUIPT technology comparable to the  $50 \text{ n}\Phi_0/\sqrt{\text{Hz}}$  resolution obtained in state-of-the-art nanoSQUIDS based on lead [31]. Another path is to exploit wide-gap superconductors [18, 32, 33] (such as vanadium or niobium) as proximitizing elements to boost the responsivity figures. The choice of the abovementioned wide-gap superconductors is also a prerequisite for withstanding the sizeable magnetic field that would be necessary for pushing the spin resolution in nanoscale loop SQUIPTs beyond the current state-of-the-art level [31]. In this respect, under optimal coupling [34], we estimate the spin resolution of our SQUIPT  $S_N = r\Phi_N/\pi\mu_0\mu_B \approx 24 \mu_B/\sqrt{\text{Hz}}$ , where  $r$  is the SQUIPT effective radius,  $\mu_0$  is the vacuum permeability and  $\mu_B$  is the Bohr magneton.

In summary, we have presented a SQUIPT device implemented with a fabrication protocol based on the mature Al-Cu technology, whose design successfully resolves the limit of the incomplete phase-driven modulation of the proximity-induced minigap. The reduced spatial extent of our SQUIPT geometry (in the micrometer range), combined with ultra-low power ( $\approx 100 \text{ fW}$ ) suggest the study of the magnetic degrees of freedom of small spin populations as a possible application for this mesoscopic

interferometer. We conclude by emphasizing that the improvement in performance achieved in just four years after the initial SQUIPT proof-of-concept demonstration put this device class already on par with the fifty-years-old SQUID technology [27, 35].

The authors acknowledge M. J. Martínez-Pérez for her contribution at the early stage of this project and for valuable discussions. The Marie Curie Initial Training Action (ITN) Q-NET 264034, the Italian Ministry of Education, University and Research (MIUR) through the program FIRB-RBFR1379UX and the European Research Council under the European Union's Seventh Framework Programme (FP7/2007-2013)/ERC grant agreement No. 615187-COMANCHE are acknowledged for partial financial support. C.A. thanks the Tuscany Region for funding his fellowship via the CNR joint project "PROXMAG".

---

\* carles.altimiras@sns.it

- [1] F. Giazotto, J. T. Peltonen, M. Meschke, and J. P. Pekola, Superconducting quantum interference proximity transistor, *Nature Physics* **6**, 254–259 (2010).
- [2] P. G. de Gennes, *Superconductivity of Metals and Alloys* (Benjamin, New York, 1966).
- [3] H. le Sueur, P. Joyez, H. Pothier, C. Urbina, and D. Esteve, Phase controlled superconducting proximity effect probed by tunneling spectroscopy, *Phys. Rev. Lett.* **100**, 197002 (2008).
- [4] B.D. Josephson, Possible new effects in superconductive tunnelling, *Physics Letters* **1**, 251 – 253 (1962).
- [5] K. K. Likharev, Superconducting weak links, *Rev. Mod. Phys.* **51**, 101–159 (1979).
- [6] R. Doll and M. Näbauer, Experimental proof of magnetic flux quantization in a superconducting ring, *Phys. Rev. Lett.* **7**, 51–52 (1961).
- [7] B. S. Deaver and W. M. Fairbank, Experimental evidence for quantized flux in superconducting cylinders, *Phys. Rev. Lett.* **7**, 43–46 (1961).
- [8] J. J. A. Baselmans, T. T. Heikkilä, B. J. van Wees, and T. M. Klapwijk, Direct observation of the transition from the conventional superconducting state to the  $\pi$  state in a controllable Josephson junction, *Phys. Rev. Lett.* **89**, 207002 (2002).
- [9] V. T. Petrashov, V. N. Antonov, S. V. Maksimov, and R. Sh. Shalkhaldarov, Conductivity of mesoscopic structures with ferromagnetic and superconducting regions, *JETP Letters* **59**, 551–555 (1994).
- [10] V. T. Petrashov, V. N. Antonov, P. Delsing, and T. Claesson, Phase controlled conductance of mesoscopic structures with superconducting mirrors, *Phys. Rev. Lett.* **74**, 5268–5271 (1995).
- [11] M. H. Devoret and R. J. Schoelkopf, Amplifying quantum signals with the single-electron transistor, *Nature* **406**, 1039–1046 (2000).
- [12] R. J. Schoelkopf, P. Wahlgren, A. A. Kozhevnikov, P. Delsing, and D. E. Prober, The radio-frequency single-electron transistor (RF-SET): A fast and ultrasensitive electrometer, *Science* **280**, 1238–1242 (1998).
- [13] F. Giazotto and F. Taddei, Hybrid superconducting quantum magnetometer, *Phys. Rev. B* **84**, 214502 (2011).
- [14] M. Meschke, J. T. Peltonen, J. P. Pekola, and F. Giazotto, Tunnel spectroscopy of a proximity Josephson junction, *Phys. Rev. B* **84**, 214514 (2011).
- [15] R. N. Jabdaraghi, M. Meschke, and J. P. Pekola, Non-hysteretic superconducting quantum interference proximity transistor with enhanced responsivity, *Applied Physics Letters* **104**, 082601 (2014).
- [16] A. A. Golubov, M. Yu. Kupriyanov, and E. Il'ichev, The current-phase relation in Josephson junctions, *Rev. Mod. Phys.* **76**, 411–469 (2004).
- [17] G. J. Dolan, Offset masks for liftoff photoprocessing, *Applied Physics Letters* **31**, 337–339 (1977).
- [18] A. Ronzani, C. Altimiras, and F. Giazotto, Balanced double-loop mesoscopic interferometer based on Josephson proximity nanojunctions, *Applied Physics Letters* **104**, 032601 (2014).
- [19] J. Bardeen, L. N. Cooper, and J. R. Schrieffer, Theory of superconductivity, *Phys. Rev.* **108**, 1175–1204 (1957).
- [20] R. C. Dynes, V. Narayanamurti, and J. P. Garno, Direct measurement of quasiparticle-lifetime broadening in a strong-coupled superconductor, *Phys. Rev. Lett.* **41**, 1509–1512 (1978).
- [21] J. P. Pekola, V. F. Maisi, S. Kafanov, N. Chekurov, A. Kemppinen, Yu. A. Pashkin, O.-P. Saira, M. Möttönen, and J. S. Tsai, Environment-assisted tunneling as an origin of the Dynes density of states, *Phys. Rev. Lett.* **105**, 026803 (2010).
- [22] P. Virtanen and T. T. Heikkilä, Thermoelectric effects in superconducting proximity structures, *Appl. Phys. A* **89**, 625–637 (2007), source code available at <http://t1.tkk.fi/~theory/usadel1/>.
- [23] J. C. Hammar, J. C. Cuevas, F. S. Bergeret, and W. Belzig, Density of states and supercurrent in diffusive SNS junctions: Roles of nonideal interfaces and spin-flip scattering, *Phys. Rev. B* **76**, 064514 (2007).
- [24] M. Tinkham, *Introduction to Superconductivity*, 2nd ed. (Dover Publications, 2004).
- [25] F. Giazotto, T. T. Heikkilä, A. Luukanen, A. M. Savin, and J. P. Pekola, Opportunities for mesoscopics in thermometry and refrigeration: Physics and applications, *Rev. Mod. Phys.* **78**, 217–274 (2006).
- [26] H. Q. Nguyen, T. Aref, V. J. Kaupilla, M. Meschke, C. B. Winkelmann, H. Courtois, and J. P. Pekola, Trapping hot quasi-particles in a high-power superconducting electronic cooler, *New Journal of Physics* **15**, 085013 (2013).
- [27] J. Clarke and A. I. Braginski, *The SQUID Handbook Fundamentals and Technology of SQUIDs and SQUID Systems*, Vol. 1 (Wiley-VCH, Weinheim, 2006).
- [28] J. Nagel, O. F. Kieler, T. Weimann, R. Wölbing, J. Kohlmann, A. B. Zorin, R. Kleiner, D. Koelle, and M. Kemmler, Superconducting quantum interference devices with submicron Nb/HfTi/Nb junctions for investigation of small magnetic particles, *Applied Physics Letters* **99**, 032506 (2011).
- [29] R. Wölbing, J. Nagel, T. Schwarz, O. Kieler, T. Weimann, J. Kohlmann, A. B. Zorin, M. Kemmler, R. Kleiner, and D. Koelle, Nb nano superconducting quantum interference devices with high spin sensitivity for operation in magnetic fields up to 0.5T, *Applied Physics Letters* **102**, 192601 (2013).
- [30] N. Beev and M. Kiviranta, Fully differential cryogenic transistor amplifier, *Cryogenics* **57**, 129 – 133 (2013).

- [31] D. Vasyukov, Y. Anahory, L. Embon, D. Halbertal, J. Cuppens, L. Neeman, A. Finkler, Y. Segev, Y. Myasoedov, M. L. Rappaport, M. E. Huber, and E. Zeldov, A scanning superconducting quantum interference device with single electron spin sensitivity, *Nature Nanotechnology* **8**, 639–644 (2013).
- [32] C. P. García and F. Giazotto, Josephson current in nanofabricated V/Cu/V mesoscopic junctions, *Applied Physics Letters* **94**, 132508 (2009).
- [33] A. Ronzani, M. Baillergeau, C. Altimiras, and F. Giazotto, Micro-superconducting quantum interference devices based on V/Cu/V Josephson nanojunctions, *Applied Physics Letters* **103**, 052603 (2013).
- [34] J. Gallop, P. W. Josephs-Franks, J. Davies, Ling Hao, and J. Macfarlane, Miniature dc SQUID devices for the detection of single atomic spin-flips, *Physica C: Superconductivity* **368**, 109 – 113 (2002).
- [35] R. C. Jaklevic, J. Lambe, A. H. Silver, and J. E. Mercereau, Quantum interference effects in Josephson tunneling, *Phys. Rev. Lett.* **12**, 159–160 (1964).